NANO · MICRO small
www.small-journal.com

Infrared-Triggered Retinomorphic Artificial Synapse Electronic Device Containing Multi-Dimensional van der Waals Heterojunctions

Soobin Shim, Seongchan Kim, Donghyun Lee, Hyeongtae Kim, Mi Ji Kwon, Su-yeon Cho, Windy Ayu Lestari, Jaeyoung Seo, Dongjoon Yeo, Jina Na, Somnath Suhas Kundale, Nuri Oh, and Jun Hong Park**

Biological systems excel in image recognition with low power and fast responses. Inspired by the human eye, researchers have developed solid-state artificial visual systems. In this study, a retinomorphic artificial synapse device based on a tungsten diselenide (WSe2)/indium arsenide quantum dot (InAs QD) heterostructure is developed. This device exhibits enhanced short-wavelength infrared (SWIR) responsivity at 1060 nm, which is a synaptic behavior analogous to the human retina. The WSe2/InAs QD improves charge transport and photon absorption through the quantum confinement effects of InAs QDs, facilitating efficient SWIR detection. The heterojunction enables effective electron–hole pair separation, enhancing the photodetector performance. The device adapts to SWIR signal pulses like the human eye to light flicker. The WSe_2/InAs QD device demonstrates significantly higher responsivity and a superior ability to emulate a wide range of synaptic properties compared to previously reported Si-based and 2D material/QD-based devices. An artificial neural network trained on the Fashion MNIST dataset achieved over 85% accuracy, which is higher than previous reports. This showcases the potential of retina-inspired SWIR optoelectronic devices for compact, efficient machine vision and in-sensor computing. This study underscores the potential of integrating QDs with 2D materials to create advanced photodetectors that mimic biological sensory functions.

1. Introduction

The human visual system comprising the retina and visual cortex plays a crucial role in perceiving information. The retina receives optical signals and converts them into electrical signals, which are transferred to the cortex via the optic nerve.[1] The biological process of visual information detection and computation occurs almost instantaneously with minimal power consumption. Inspired by this efficient sensory mechanism, researchers have developed artificial visual systems for solid-state applications.[2] These artificial visual systems approximate the synaptic functions and neural connectivity of human vision, as observed in retina-inspired devices.[3] Moreover, researchers have developed biomimetic optoelectronic synapse transistors that detect and process infrared (IR) signals, similar to the biological sensory behavior of perceiving and processing input optical stimulation.[4] These transistors have been used in autopilot technologies, telecommunications,

S. Shim, H. Kim, M. J. Kwon, W. A. Lestari, J. H. Park
Department of Materials Engineering and Convergence Technology
Gyeongsang National University
Jinju, Gyeongsangnam-do 52828, Republic of Korea
E-mail: yakte@gnu.ac.kr

S. Kim, J. Seo, D. Yeo, J. Na, N. Oh
Division of Materials Science and Engineering
Hanyang University
222, Wangsimni-ro, Seongdong-gu, Seoul 04763, Republic of Korea
E-mail: irunho@hanyang.ac.kr

D. Lee
Department of Electrical Engineering
Yale University
New Haven, CT, USA

S.-yeon Cho, J. H. Park
School of Materials Science and Engineering
Gyeongsang National University
Jinju, Gyeongsangnam-do 52828, Republic of Korea

S. S. Kundale, J. H. Park
Research Institute for Green Energy Convergence Technology
Gyeongsang National University
Jinju, Gyeongsangnam-do 52828, Republic of Korea

The ORCID identification number(s) for the author(s) of this article can be found under https://doi.org/10.1002/smll.202410892

DOI: 10.1002/smll.202410892

and light detection and ranging (LiDAR).[5] Consequently, the demand for processing units with ultrasensitive photoresponses beyond the Si detection range (>1000 nm), as in-sensor computing and edge computing, has been increasing.[6] Despite their widespread use, silicon-based optoelectronic devices face critical challenges, including limited detection wavelength ranges, high power consumption, low integration density, and suboptimal structural uniformity and stability. These limitations hinder their applicability in advanced neuromorphic and optoelectronic systems.[7]

An ideal biomimetic retina-inspired device should contain a semiconductor channel with ultrafast responses and a large dynamic range upon optical stimulation. Layered transition metal dichalcogenides (TMDs), with their ultra-thin body channels and tunable bandgaps,[8] are potential candidates for the semiconductor platforms used in retina-inspired electronics. The thin, layered structures of TMDs endow them with excellent electrostatic performance and phonon propagation, which is advantageous for synaptic devices and photodetectors. According to the vdW stacking strategy, IR-absorbing layers can act as receptors and convert optical stimulation into electrical signals, which are then propagated by TMDs and processed via computation. To achieve electronic sensitivity to IR wavelengths greater than 1000 nm, the active layer (artificial retina) should have a narrow bandgap (below 1.2 eV). However, monolayer TMDs have bandgaps in the range of 1.57–2.03 eV,[9] which lead to low carrier mobility, low output current, and low photoresponse.

Conversely, colloidal quantum dots (QDs) have emerged as promising materials for achieving the desired IR photoresponses owing to their unique optical and electronic properties, including bandgap modulation.[10] QDs possess a high absorption coefficient, enabling efficient photon capture, multiple electron-hole pair generation, and rapid carrier relaxation times, which result in fast responses.[11] Among QDs, indium arsenide (InAs) QDs have emerged as the most promising materials for exhibiting the desired IR photoresponses. Unlike PbS or Hg-based QDs, which have environmentally regulated elements, InAs QDs have small carrier effective masses, large exciton Bohr radii, and direct bandgaps, enabling precise control over their optical properties and precise tuning of the absorption and emission wavelengths.[12] Hence, InAs QDs could push photodetection boundaries. Compared to previous studies on 2D materials and QDs in optoelectronic synaptic devices, it was observed that most of these materials barely exhibit multiwavelength photosynaptic responses critical for synaptic functionality. A detailed comparison of their performance is provided in the Supporting Information and summarized in Table S1.

In this study, we stacked InAs QD layers as artificial retinal receptors on a tungsten diselenide (WSe_2) synapse device to enhance the short wavelength IR (SWIR) responsivity and synaptic behavior of the device consistent with retinomorphic transistors based on multi-dimensional heterojunctions.[13] The WSe_2 channel structure would afford efficient charge transport, whereas InAs QDs would exhibit quantum confinement effects to enhance IR photon absorption, resulting in improved detection.[14] The WSe_2/InAs vdW heterojunction device was engineered to exhibit sensitivity across a wide range of IR wavelengths over 1000 nm.[15] A heterojunction with effectively separated photoexcited electron-hole pairs would enhance the performance of the photodetectors.[16] The device achieves a remarkable responsivity of 1.134 A/W and exhibits superior synaptic properties, including robust photocurrent switching (PSC), spike-timing-dependent plasticity (STDP), long-term potentiation/depression (LTP/LTD), and paired-pulse facilitation/depression (PPF/PPD). Furthermore, the WSe_2/InAs retinomorphic synapse adapts to short-wavelength infrared (SWIR) pulse signals, closely mimicking the human eye's ability to adjust to changes in ambient light intensity. Notably, the neuromorphic characteristics of photoreactive transistors in the IR region have remained largely unexplored. This study systematically investigates these properties, contributing to a deeper understanding of their potential in neuromorphic applications. Furthermore, we trained an artificial neural network (ANN) and achieved a high inference accuracy of the image recognition rate for the Fashion MNIST dataset, which is encoded into spikes by the device.[17] Therefore, retina-inspired optoelectronic devices, which integrate perception and encoding functionalities, can perform SWIR-triggered computation in a highly compact and efficient manner, enabling in-sensor computing.[18]

2. Results and Discussion

For efficient IR absorption beyond the 1000 nm region, InAs QDs were synthesized using $InCl_3$, $AsCl_3$, oleylamine, and reducing agents through co-reduction and heat-up methods.[19] We utilized a 2D-QD heterojunction structure, building on the foundation of previously reported designs.[13b] Instead of traditional infrared absorption layers that typically rely on heavy metal-based materials, we opted for InAs QDs, known for their low toxicity and absence of heavy metals. Additionally, the carrier transport properties at the WSe_2/InAs interface were enhanced by performing a ligand exchange on the surface of InAs using 1,2-ethanedithiol (EDT).[13b] The transmission electron microscopy (TEM) image of the synthesized InAs QDs (**Figure 1a**) revealed a uniform size distribution with an average diameter of 5.08 ± 0.42 nm (inset of Figure 1a). The InAs QDs (Figure 1b) exhibited X-ray diffraction (XRD) peaks at 25.4°, 42.2°, and 50°, corresponding to the (111), (220), and (311) planes of the zinc-blende lattice structure of bulk InAs. Figure 1c shows the Raman spectra of WSe_2, InAs, and WSe_2/InAs at an excitation wavelength of 532 nm. The sharp peak at 520 cm^{-1} corresponds to the Si substrate. Bare WSe_2 exhibited the characteristic Raman modes E^1_{2g} and B^1_{2g} at 249.1 and 306.1 cm^{-1}, respectively. Additionally, the three peaks at ~355, 371, and 393 cm^{-1} are consistent with the expected Raman modes for WSe_2.[20] Bare InAs QDs exhibited distinct peaks at 217.3 and 231.2 cm^{-1}, corresponding to the InAs Raman peaks.[21] By controlling the reaction temperature, we tuned the size of InAs QDs, achieving a 1st exciton absorption peak in the IR region, ranging from 940 to 1100 nm (from 1.3 to 1.1 eV) (Figure 1d).[19] Additionally, the band energy levels of the InAs QD films and WSe_2 were confirmed using ultraviolet photoelectron spectroscopy (UPS) (Figure 1e). Prior to the UPS measurements, solid-state ligand exchange using 1,2-ethanedithiol (EDT) was performed to improve the electrical properties of the InAs QDs by reducing their dot-to-dot distance. The band edge

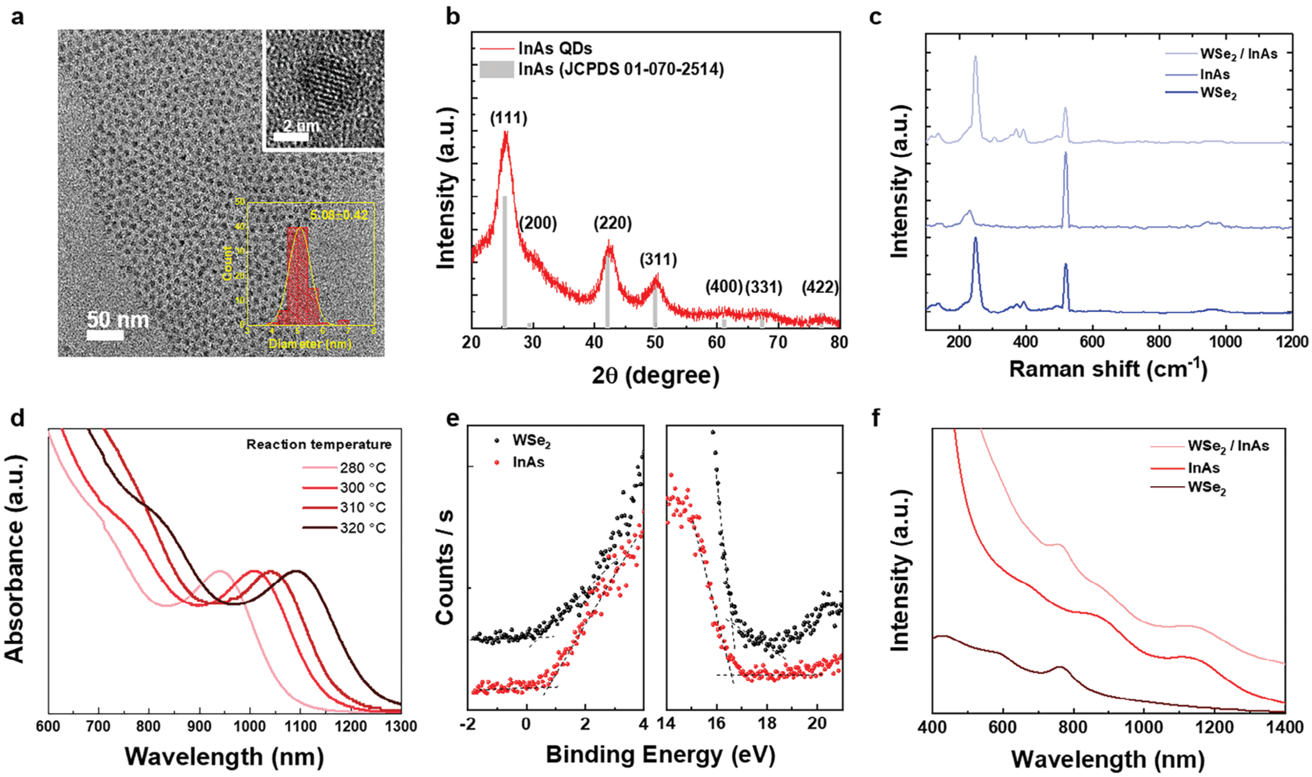

Figure 1. Material characteristics of indium arsenide quantum dots (InAs QDs) and tungsten diselenide (WSe_2)/InAs heterojunction. a) Transmission electron microscopy image of InAs QDs [inset: high-resolution transmission electron microscopy image of InAs QDs and the histogram of the size distribution]. b) Comparison of the X-ray diffraction patterns of InAs QDs and JCPDS 01-070-2514. c) Raman spectra of WSe_2, InAs, and WSe_2/InAs heterojunctions. d) Ultraviolet-visible near IR (UV-vis-NIR) absorption spectra of InAs QDs synthesized at different reaction temperatures. e) Ultraviolet photoelectron spectra of InAs QDs and WSe_2. f) UV-vis-NIR absorption spectra.

position of InAs QDs treated with EDT were calculated using the following equations.

$$W_F = 21.22 - \left(E_{cutoff} - E_F\right)(eV) \tag{1}$$

$$VBM = 21.22 - \left(E_{cutoff} - E_{cutonset}\right)(eV) \tag{2}$$

where E_{cutoff} is the secondary electron cutoff, E_F is the Fermi level, VBM is the valence band maximum, and $E_{cutonset}$ is the onset energy in the valence band region. The E_{cutoff} and $E_{cutonset}$ values of the EDT-treated InAs QD film were 16.68 and 0.74 eV, respectively. Consequently, the calculated VBM of the InAs QDs was −5.28 eV. The conduction band minimum (CBM) was calculated to be −4.3 eV from the Tauc plot. The extracted work function level was −4.54 eV, which indicates that the EDT-treated InAs QDs possessed n-type characteristics. Furthermore, the E_{cutoff} and $E_{cutonset}$ values of WSe_2 were 16.5 and 0.44 eV, respectively. The calculated VBM and CBM of WSe_2 were −5.16 and −3.95 eV, respectively. Figure 1f shows the ultraviolet-visible near IR absorption spectra of WSe_2, InAs, and WSe_2/InAs. The WSe_2 spectrum shows peaks at 587 and 762 nm, which are consistent with the direct excitonic transition of WSe_2.[22] The first excitonic peak of the InAs QDs is observed at 1130 nm, which enables absorption in the SWIR region. The WSe_2/InAs heterojunction spectrum shows peaks corresponding to both WSe_2 and InAs QDs, which suggests the absence of physical changes during the formation of the heterojunction.

The photodetection capabilities of synaptic devices of 0D/2D vdW heterojunctions irradiated with a 1060 nm laser have been attributed to the integration of absorbing materials with different energy bandgaps and the formation of built-in electric fields.[23] We fabricated a bare WSe_2 device via a thermal chemical vapor deposition (CVD) method[24] using an e-beam evaporator. Ni electrode material, which provides electron-hole carrier pathways, was deposited on a SiO_2/Si substrate. Subsequently, WSe_2 was deposited on the substrate. To mimic the human retinal photoresponse to SWIR, InAs QDs were spin-coated on the resultant substrate (**Figure** 2a We performed elemental analysis on the cross-sectional WSe_2/InAs van der Waals (vdW) heterojunction device using energy-dispersive X-ray spectroscopy (EDS). The results confirm that ≈30 nm thick WSe_2 was uniformly layered beneath ≈16 nm of InAs QDs. High-resolution TEM (HRTEM) images reveal the interplanar spacing of the (002) plane of WSe_2 and the (111) plane of InAs, verifying the formation of a heterojunction structure (Figure 2b). Furthermore, the EDS analysis shows that W, Se, In, and As elements are uniformly distributed within their respective regions, with a clear and distinct interface observed between the WSe_2 and InAs QD layers (Figure 2c). Additionally, SEM-EDS analysis was conducted to further investigate the elemental distribution of the planar WSe_2/InAs vdW heterojunction device, as shown in Figure S1. The WSe_2/InAs heterojunction

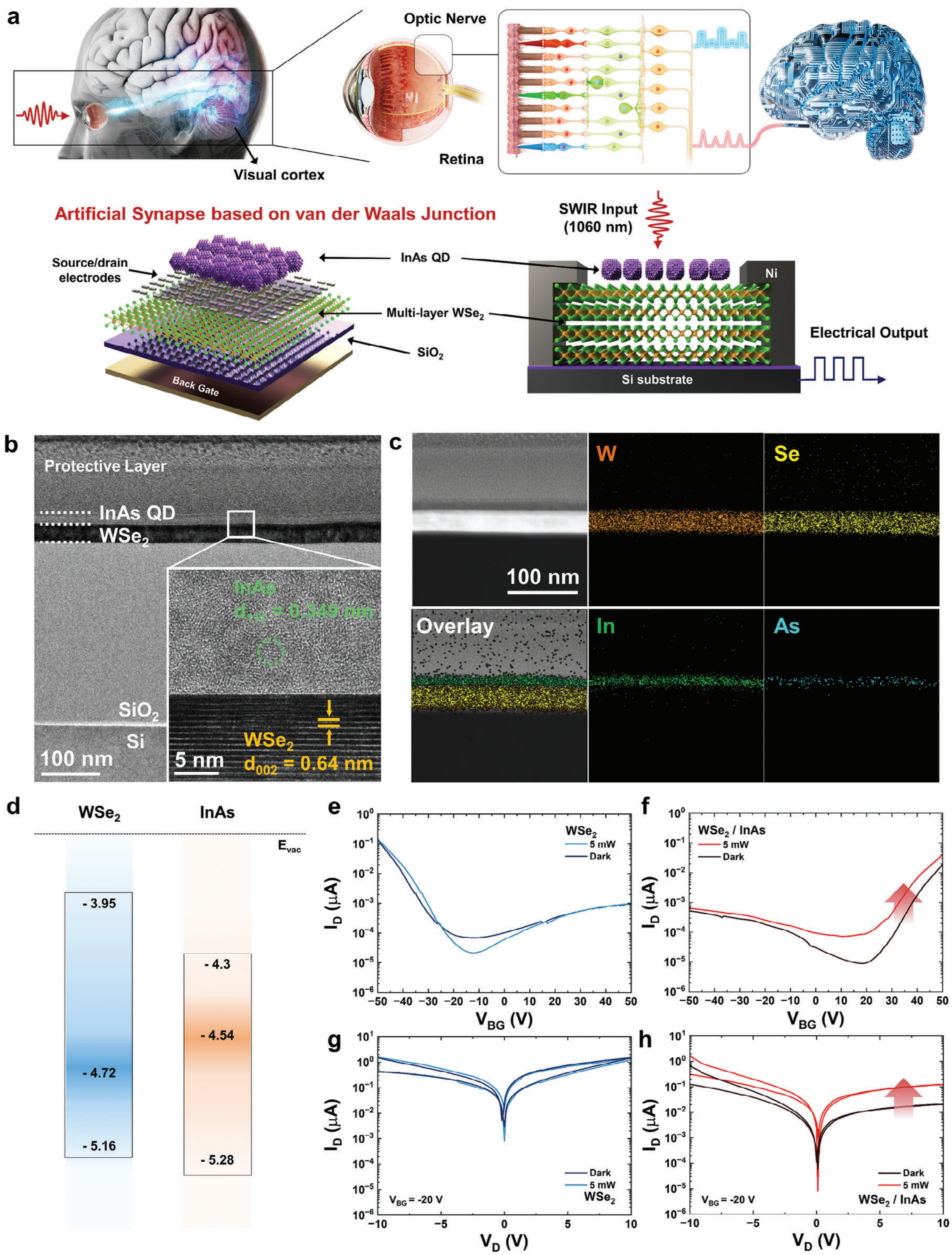

Figure 2. Electrical transport properties of the WSe_2/InAs van der Waals (vdW) heterojunction device. a) Conceptual schematic of a retinomorphic device. b) cross-sectional TEM images of WSe_2/InAs van der Waals (vdW) heterojunction device (inset: high-resolution TEM image), and c) corresponding elemental mapping of WSe_2/InAs vdW heterojunction device, illustrating the distributions of W (orange), Se (yellow), In (green), and As (cyan). d) WSe_2/InAs band structure determined from ultraviolet photoelectron spectroscopy and a Tauc plot. Transfer characteristics of the e) WSe_2 and f) WSe_2/InAs vdW heterojunction device in the dark and under 5 mW illumination (gate voltage: −50 to 50 V, drain voltage: 1 V). Output characteristics of the g) WSe_2 and h) WSe_2/InAs vdW heterojunction device in the dark and under 5 mW illumination at a gate voltage of −20 V.

was analyzed under 1060 nm laser irradiation. The bandgaps of WSe_2 and InAs QDs (Figure 2d) were determined to be ≈1.21 and 0.98 eV, respectively, at room temperature (Figures 1e and S2). Excitation at 1060 nm generated electron-hole pairs within the QD absorber layer, which were transported to the WSe_2 channel, leading to photocurrent generation.

The differences in the energy bandgaps and work functions of various TMDs facilitate the formation of type-II band alignments and the establishment of suitable built-in electric fields at the heterointerfaces. Notably, the bandgaps and work functions of TMD and QDs vary with the number of layers and sizes, respectively. Therefore, we further tuned the band alignment at the WSe_2/InAs heterointerface by considering the number of individual WSe_2/InAs layers in the vdW heterostructure. For this, the work function of the device surface after InAs QD deposition was investigated and modified using scanning Kelvin probe microscopy (SKPM) (Figure S3). The investigation of the work function in the same region before and after the deposition of InAs revealed a significant increase in the work function value. This change in surface charge distribution, combined with the results of the band structure, more strongly predicts that the device may exhibit n-type characteristics due to the deposition of QDs. The transfer characteristics of the fabricated WSe_2 field effect transistors (FETs) were compared in the dark and under different powers of the 1060 nm laser. The deposition of InAs QDs resulted in a type-II heterojunction, which enhanced the transfer of photogenerated electrons and holes at the CBM and VBM of the p-type and n-type InAs QDs, respectively. The spatial separation of the photogenerated electrons and holes increased their lifetime, lowering the electron-hole recombination rate and establishing a stronger intrinsic electric field. Consequently, an improved photoresponse was observed in both photovoltaic and photoconductive modes, with or without an external bias. This is attributed to the interlayer photoexcitation process, which reduces the energy differences between the electrons and holes located at the spatially separated CBM and VBM in the type-II heterointerface. Additionally, the vdW heterostructure exhibited a significant photoresponse to incident light at the natural bandgaps of the WSe_2 and InAs constituents. Trap sites at the 0D-2D interface capture photogenerated electrons and holes, altering the potential energy of the interface. This charge-trapping effect significantly influences synaptic plasticity and is crucial for the memory function of photosynthetic transistors.[25]

When a V_{BG} range of −50 to +50 V was applied to the pristine WSe_2 device, photogenerated charge carriers accumulated at the SiO_2/WSe_2 interface and were captured by trap sites on the SiO_2 surface, which reduced the output current. Pristine WSe_2 exhibited weak p-type behavior owing to the dangling bonds on the SiO_2 surface and unintentional Se vacancies, which is consistent with the results shown in Figure 2e. In contrast, when a negative V_{BG} was applied to the pristine WSe_2 device, the trapped photogenerated charge carriers were released into the channel, increasing the output current. However, depositing the n-type InAs QDs/EDT layer on the p-type WSe_2 channel layer changed the transfer curve from p-type to n-type (Figure 2f).[26] The n-type InAs QDs affected the major charge carriers involved in the transfer process during the device operation. InAs QDs possess ligands, which can trap the primary carriers flowing through bare WSe_2 when the QDs cover it, hindering their smooth movement. Additionally, InAs QDs are electrically n-type, so when a gate bias is applied during measurement, the majority carriers, which are electrons, are drawn towards the TMD surface. These accumulated electrons are injected into the conduction channel of WSe_2, resulting in the observation of n-type electrical characteristics.[27] Output characteristics of the WSe_2 device were measured in the dark with a drain bias of −10 to 10 V and a gate bias of −20 V (Figure 2g).[28] In comparison, the photodetecting device exposed to the 1060 nm laser exhibited a broader current range than that of the pristine device at the same gate bias −20 V (Figure 2h). The output curves at a gate bias of −20 V in the dark and under SWIR illumination revealed the injection of electrons by InAs QDs into the WSe_2 channel (Figure S4, Supporting Information). Furthermore, the effectiveness of the EDT solution in replacing the ligand was evaluated by measuring the relevant properties of WSe_2 after applying the solution. The introduction of the QDs changed the electrical characteristics of the device (Figure S5, Supporting Information). The WSe_2/InAs heterojunction structure overcame the limitations of photodetectors under SWIR illumination.

The incident photon energy from the SWIR laser stimulated the InAs QDs and enhanced the charge transfer at the WSe_2/InAs interface (**Figure 3a**). The responsivity (R) and detectivity (D^*) of the device were measured under 1060 nm laser illumination. The two indices reflect the conversion of electrical conductivity to photoresponse ability. Responsivity is expressed as follows:[29]

$$R = \frac{I_{Ph} - I_{dark}}{P_{in}\,A} \tag{3}$$

where I_{dark} is the on-current in the transfer curve without the 1060 nm laser, I_{ph} is the photocurrent, P_{in} is the illumination induced density, and A is the photo-activated channel area. The channel area was maintained at a fixed dimension of 150 μm^2. Figure 3b shows the calculated values of R and D* under 12.99 mW/cm^2 (5 mW) SWIR illumination density, with the maximum values detected at various back-gate voltages. Compared to the pristine WSe_2 device, the heterojunction device exhibited ∼43 times higher light response characteristics. Responsivity measures the sensitivity of a photodetector to the incident light and indicates the amount of photocurrent generated per unit of incident optical power. Detectivity measures the ability of the device to detect weak signals, considering both responsivity and noise characteristics. Detectivity is expressed as follows:[29]

$$D^* = \frac{R}{\sqrt{\frac{2qI_{dark}}{A}}} \tag{4}$$

where A is the channel dimension of the photodetector, and D^* depends on R.

Such changes in charge distribution contributed to an additional electric gating field, thus changing the charge-transport behavior including a shift in the threshold voltage (V_{TH}). The trapped charges clearly distinguished the drain current under dark and light exposure conditions. A comparison of R and D* under a 5 mW power of 1060 nm illumination is shown in Figure 3b. Furthermore, the device showed the highest responsivity among those of similarly structured devices in the

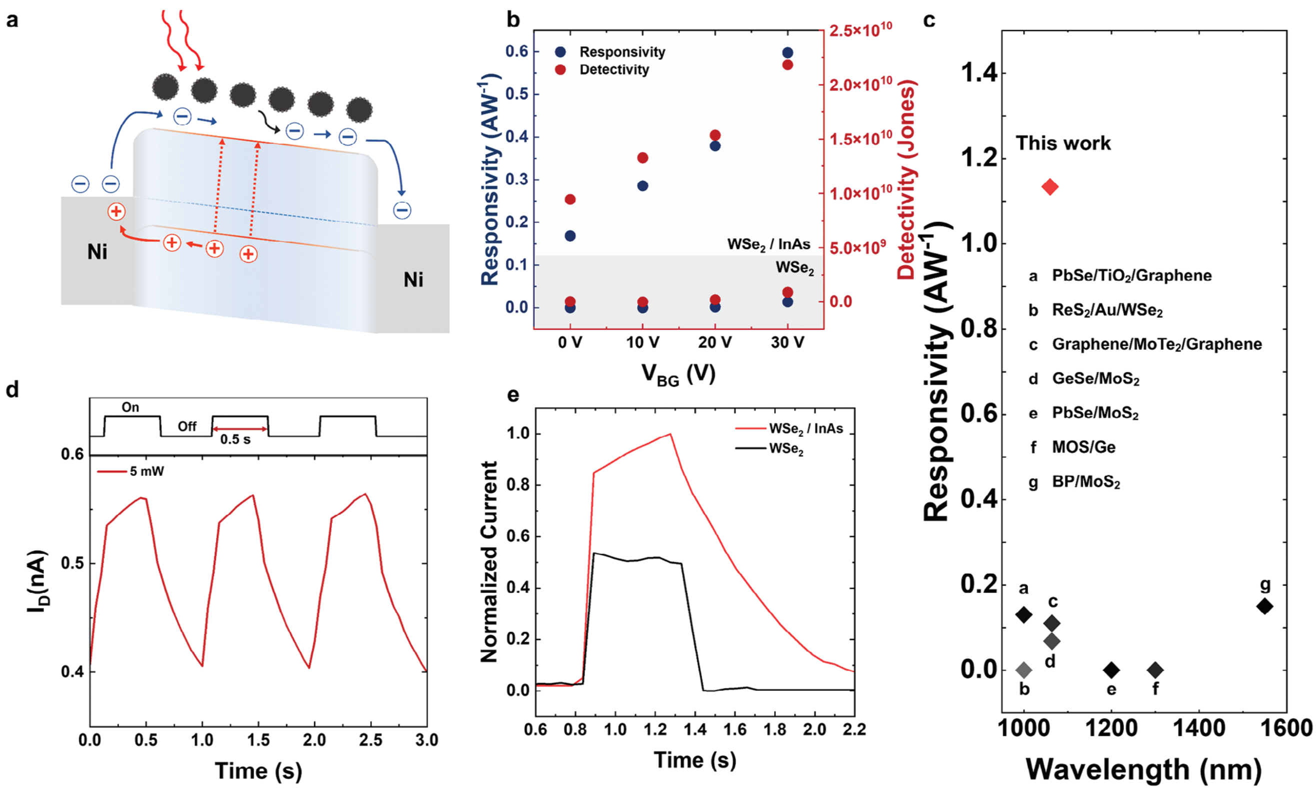

Figure 3. Electrical transport properties of the WSe_2/InAs vdW heterojunction device. a) Illustration of the WSe_2/InAs vdW heterojunction device under 1060 nm laser illumination, where QDs enhance charge transfer. b) Responsivity and detectivity of the bare WSe_2 and WSe_2/InAs FET under 12.99 mW cm^{-2} (5 mW) illumination. c) Comparison of the responsivities of our device and previously reported devices. d) Response time of the WSe_2/InAs vdW heterojunction device under a 5 mW laser. e) Comparison of the response times of the WSe_2 and WSe_2/InAs vdW heterojunction device.

nearby wavelength range (Figure 3c).[30] We compared the responsivity by selecting devices with heterostructure configurations from previously reported papers. The details of specific values are summarized in Table S2, Supporting Information. We investigated the repetitive photoresponse of the WSe_2/InAs vdW heterojunction device by application of three continuous optical pulses (pulse width 0.5s and power 5 mW) as shown in Figure 3d. Then we compared the WSe_2 and WSe_2/InAs vdW heterojunction device photoresponse with the same optical pulse parameter and it was found that the heterojunction device has higher photoresponse and fast response time than that of the pristine WSe_2 device (Figures 3e). Also, it is noted that the recovery time of WSe_2/InAs vdW heterojunction device is longer than WSe_2 device which can be suitable to improve the long-term memory property of the device. This suggests that the memory of the WSe_2/InAs vdW heterojunction device was quicker than that of the WSe_2 device. In addition, the more pronounced decreasing decay speed of the WSe_2 device suggests that the WSe_2/InAs vdW heterojunction device has a higher memorizing efficiency than that of the WSe_2 device. For neuromorphic applications, mobile carriers in the devices need to be more trapped. As a result, more trapped carriers make the low inclination. On the other hand, to get good quality and clearer photoresponsivity, the devices need to respond rapidly by optical stimulation. Figure 3d shows that the device maintains a high speed in the increasing area. Thus, the incorporation of IR-absorbing InAs QDs into the photodetector device enhanced the photoresponse speed. Furthermore, the rapid increase followed by a decline in conductivity of the WSe_2/InAs vdW heterojunction device indicated an active photoresponse, which is beneficial for learning characteristics.

First, we investigated whether WSe_2/InAs vdW heterojunction device could be considered potential neuromorphic devices. Figure S6 shows an increase in hysteresis after QD deposition. This substantial hysteresis effect contributes to an enhanced noise tolerance and reduced variability in the transistor response, facilitating more stable and accurate synaptic weight updates. In order to investigate whether the device can mimic the function of a human retina, we conducted experiments using a light pulse with a learning-and-forgetting sequence. Previously, to verify the responsiveness of the device to a light pulse, we applied a single pulse and observed the photoreactivity in **Figure 4a**. As the intensity of the photogenerated charges increased, The EPSC increased proportionally with the number of light pulses, corresponding to the accumulation of photogenerated charges. The blue line represents the EPSC response to a single light optical pulse, while the red line illustrates the response to three consecutive pulses (Figure 4b). These results demonstrate the device's potential to emulate learning and forgetting processes under optical stimulation. To further establish the correlation between pulse and EPSC, we examined the increase in current level with the number of pulses previously

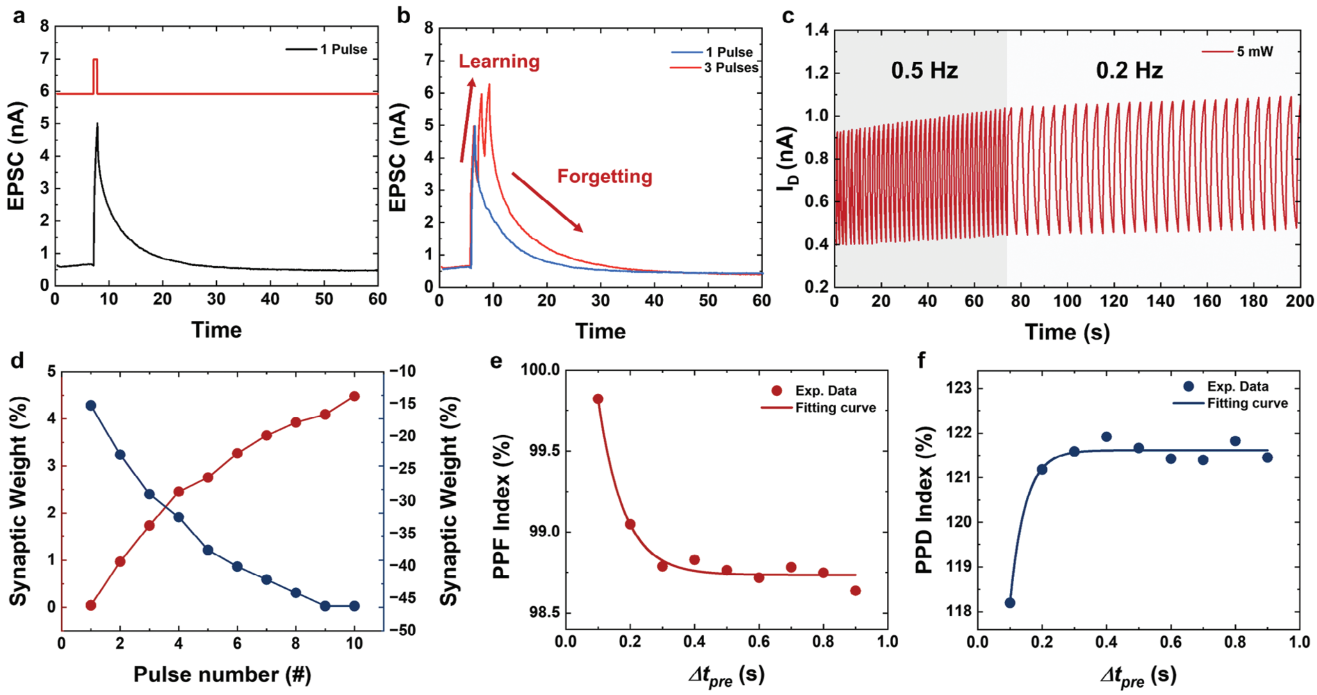

Figure 4. Neuromorphic characteristics of the InAs/WSe_2 artificial synapse device. a) Excitatory postsynaptic current (EPSC) response stimulated by 1060 nm laser illumination. b) EPSC is stimulated by a single (blue) pulse and three (red) optical pulses. c) Long-term potentiation (LTP) of the WSe_2/InAs FET with 0.5 and 0.2 Hz laser frequency at 5 mW illumination power. d) Synaptic weight of the WSe_2/InAs vdW heterojunction device at 11 pulses under 5 mW illumination. Electrical programming of synaptic weights: e) paired-pulse facilitation (PPF) indices from potentiation at various interval times and f) paired-pulse depression (PPD) indices from depression under various interval times under 5 mW illumination.

investigated, and in Figure S7, Supporting Information, we confirmed the increase in EPSC level with pulse width (35,50 and 100 ms). After the pulse ceased, the EPSC gradually returned to its initial state owing to the slow recombination of trapped electrons and holes.[31] Moreover, additional optical synaptic experiments were conducted based on these characteristics, which allowed comparison with other studies (Table S1, Supporting Information). The device exhibited good responsivity across a broad wavelength range, particularly at 450 nm and 1060 nm. Furthermore, our methodology includes rare analyses such as spike-timing dependent plasticity (STDP) and Fashion MNIST. Deposing InAs QDs enhance not only the responsivity by making more n-type properties but also since ligands of QDs make more trap sites our reported device can be optimized neuromorphic properties at the same time. The deposition of QDs not only enhances photoreaction properties but can also show their application to neuromorphic devices at the same time. The trap sites formed by ligands have the ability to capture charges. This is similar to the mechanism of releasing and absorbing neurotransmitters in biological synapses. The more trap sites there are, the more charges can be stored, which means that various conductance states can be implemented. This has influenced the STDP characteristics that will be described later. Additionally, even during the period when external optical stimulation disappears, the carriers trapped by the trap sites for a certain period help mimic long-term memory. This plays an important role in the transition from STP to LTP. This illustrates the device's adaptability to a range of retina-inspired optoelectronic devices. Subsequently, several additional optical pulses were applied to identify the frequency changes in long-term potentiation (LTP).[32] Despite a sudden change of frequency from 0.2 to 0.5 Hz at a laser power of 5 mW (Figure 4c), the device responded with measurable LTP. It is noted that the InAs QD is deposited on WSe_2 to demonstrate IR-triggered synaptic behavior under irradiation of low-intensity IR laser, while maintaining carrier transport behavior in WSe_2 channel. Therefore, the present QD layer is about 16 nm on WSe_2, consistent with limiting absorption capacity for optical stimulation.[13c] In instances where the laser power is elevated from 5 mW to 15 mW, a decline in the photocurrent of WSe_2/InAs vdW heterojunction device has been observed. This phenomenon can be attributed to the saturating the generation of photo-induced carrier as shown in Figure S8, Supporting Information. An investigation was conducted under a 405 nm laser, which revealed that depositing QDs on pristine WSe_2 improved the photoresponse. Increasing the laser power during the irradiation of pristine WSe_2 reduced the photoresponse current (Figure S9, Supporting Information). In contrast, the heterojunction device with QD deposition exhibited an increased photoresponse. This suggests that visible-light laser irradiation of the device after InAs deposition increased its photoreactivity. Notably, our device demonstrated increased photoreactivity in both the infrared- and visible-light regions. These findings indicate that visible-light stimulation of the existing 2D/QD heterojunctions is possible and has a wide range of applications. Furthermore, the phenomena of learning and forgetting were observed under the 405 nm blue laser and applied optical pulses (Figure S10, Supporting Information). Learning and forgetting can be attributed to the ligands of InAs QDs, which trap electrical charges, enhancing synaptic behavior. The ligand traps and accumulates the charges near the QDs, expanding the memory window.[34] The WSe_2/InAs vdW heterojunction device exhibits enhanced responsivity and synaptic behavior under blue visible-light illumination (405 nm), which confirms its ability to detect a wide range of illumination. Our findings reveal the potential optoelectronic applications of WSe_2/InAs vdW heterojunction device, considering their adaptable response across diverse wavelength regions (Figure S11, Supporting Information). Additionally, the investigation of LTP and long-term depression (LTD) in pristine WSe_2 devices at varying frequencies within the SWIR regime revealed the absence of significant learning and forgetting (Figures S12 and S13). The dynamic range (DR) can be calculated using the following equation:[35]

$$DR = G_{max} / G_{min} \tag{5}$$

where the G_{max} and G_{min} are estimated from LTP and LTD, respectively. At the light frequencies of 0.1 Hz, the DR of the LTP and LTD were as low as 1.20 and 1.81, respectively based on the equation. However, the DR can be sufficiently increased by the substitution of different ligands.

The synaptic weight change resulting from pulse application was calculated as follows:

$$Synapticweight = \frac{A_n - A_1}{A_1} \times 100 \tag{6}$$

The electrical conductance factors (A_1 and A_2) were derived from the post- and pre-optical pulses, respectively. Figure 4d shows the dependence of synaptic weight changes on the number of pulses.[35] The calculation of synaptic weights demonstrates a comparable learning ability to that of biological synapses. Based on these characteristics, paired-pulse facilitation (PPF) and paired-pulse depression (PPD) were measured at various intervals between the two twin pulses (Figures 4e,f). PPF and PPD characteristics represent the dynamic reduction/enhancement of neurotransmitter release, which is a fundamental component of the transmission of information within the bio-synapse.[36] PPF was defined using pulse pairs at different intervals at constant pulse width as follows:

$$PPF\,(PPD) = \frac{\Delta PSC\ peak}{PSC_1} \times 100\% \tag{7}$$

The PPF index is expressed as the ratio of the postsynaptic response to the second presynaptic spike to the synaptic response to the first spike. For the WSe_2 device without InAs QDs, the synaptic weight was saturated even with a laser power of 5 mW at 1060 nm (Figure S14, Supporting Information). The relationship between the extracted PPF and PPD indices and the pre-stimulus interval (Δt_{pre}) can be approximated well by an exponential curve.

Programmable synaptic weights enabled the demonstration of STDP learning rules in the WSe_2/InAs FET.[37] STDP augmented the Hebbian synaptic plasticity and underpinned learning and memory by competitively modulating the strength of synapses within the neural network. The pulse width was quantified by adjusting the intervals between the pre- and postsynaptic pulses at a fixed duration of 0.5 s. The specific conditions based on the Hebbian learning rules are shown in **Figure 5a**. The synaptic weights changed depending on voltage and time, affecting the conductance of the active material based on the temporal relationship between the pre- and postsynaptic elements. The timing of the postsynaptic and presynaptic optical pulses as a function of Δt is illustrated in Figure 5b. The electrical conductance corresponding to synaptic weights ($\Delta G/G_0$) was calculated as follows:[37a]

$$\frac{\Delta G}{G_0} = \frac{G - G}{G_0} = \Delta w \tag{8}$$

where G_0 is the current observed immediately before the application of the first optical pulse, that is, the presynaptic pulse, and G is the current observed after the postsynaptic optical pulse. The $\Delta G/G_0$ data points were fitted to a line. The symmetric anti-Hebbian learning rule was obtained when both pre- and postsynaptic stimuli were applied. Symmetric Hebbian and anti-Hebbian characteristics were fitted using Gaussian functions, whereas antisymmetric-Hebbian and antisymmetric anti-Hebbian characteristics were fitted using exponential functions.[37a]

$$y = y_0 + Ae\,\frac{\left(x - x_c\right)^2}{2w^2} \tag{9}$$

$$y = y_0 + A_1\, e^{-x/t_1} \tag{10}$$

Symmetric Hebbian characteristics were observed for both the pre- and postsynaptic stimuli at a positive back-gate bias of +20 V (Figure 5c). Similarly, symmetric anti-Hebbian characteristics were observed at a back-gate bias of −20 V (Figure 5d). The Gaussian fitting curves revealed that both characteristics were symmetrically formed concerning $\Delta t = 0$. The tau factor (τ) defines how synaptic changes (potentiation or depression) decay or grow based on the Δt between pre- and postsynaptic spikes. In this study, τ determined the extent and duration of synaptic modifications and significantly influenced the learning and memory processes. The data of the antisymmetric Hebbian and anti-Hebbian rules (Figures 5e,f) were generated by applying optical spikes at the two back-gate biases of −20 and +20 V. The data were symmetrical for the origin. Implementing the learning rules enhanced the capacity of the ANN to address complex scenarios and improved the efficiency of their learning processes. The STDP results indicated that applying pulses affords more flexible responses.

To evaluate the image recognition ability of the WSe_2/InAs vdW heterojunction device under a continuous current, a series of experiments involving depression and potentiation were conducted. The voltage was set to −20 V, and 100 optical pulses were applied. Subsequently, the voltage was immediately adjusted to +20 V, while maintaining the optical pulses. Stable potentiation and depression were observed even after 100 optical pulses (**Figure 6a**).[38] The observed increase in the linearity value with continued operation can be attributed to the enhanced mobility of hot electrons in n-type InAs, as evidenced in prior studies.[39] Improved charge mobility reduces the signal distortion due to the optical pulses, thus increasing signal fidelity and enhancing linearity. The linearity resulting from the more stable responsiveness of the synaptic device developed in this study indicates that it can behave similarly to biological mechanisms. Reports related

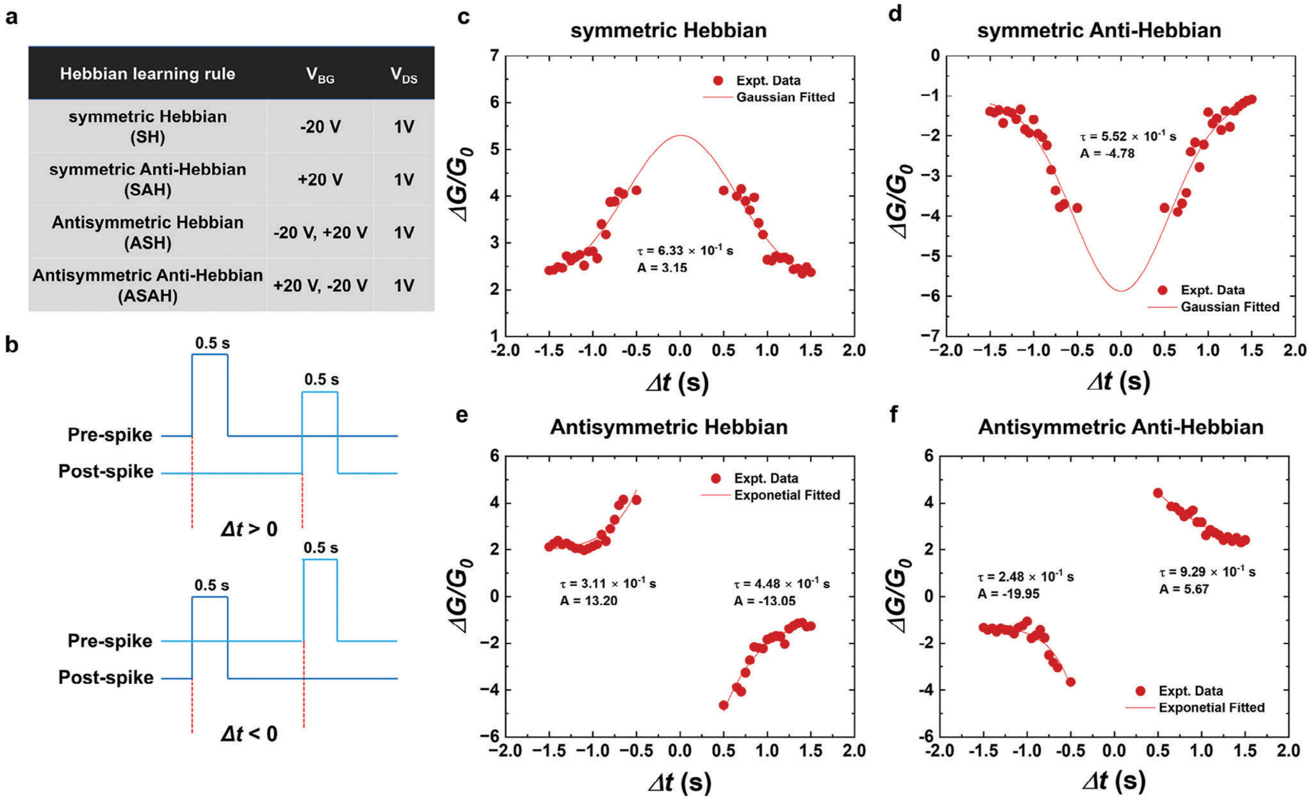

Figure 5. Four optical programming synaptic weights of the WSe_2/InAs synapse device. Emulation of Hebb's spike-timing-dependent plasticity rules using electrical pre- and postsynaptic pulses. a) Measurement setting values dependent on Hebbian learning rules. b) Illustration of optical pre-spike and post-spike at $\Delta t > 0$ and $\Delta t < 0$, respectively. c) Symmetric Hebbian, d) symmetric anti-Hebbian, e) antisymmetric Hebbian, and f) antisymmetric anti-Hebbian learning rules.

to action potentials in actual biological synapses also show that mechanisms enhancing the fidelity of neural signals can increase the stability of synaptic signal transmission.[40] To demonstrate the visual adaptive capacity of the proposed device, we used the device to classify images from the Fashion MNIST dataset.[41] The dataset contained 50000 training and 10000 test static images of 28×28 pixels related to 10 different fashion items. Figure 6b shows the ANN architecture of the Fashion MNIST dataset. The ANN comprised three multi-layer perceptron (MLP) layers with 768, 200, and 10 neurons. Each image of the Fashion MNIST dataset was flattened before being embedded into the MLP layers, and the ANN was trained by adjusting the LTP and LTD. The LTP and LTD conductance values were normalized to a range of 0.0–0.1 (Figure 6c) to make them suitable for the ANN weights. The linearity of the pristine WSe_2 device was less optimal (Figure S15). The synaptic weights (w) were further refined by approximating LTP/LTD using the following equations:[41]

$$G^{+} = G^{+}_{min} + \frac{G^{+}_{max} - G^{+}_{min}}{1 - e^{-\nu^{+}} \cdot P_{max}} \cdot \left(1 - e^{-\nu^{+}} \cdot P\right) + \sigma \tag{11}$$

$$G^{-} = G^{-}_{min} + \frac{G^{-}_{max} - G^{-}_{min}}{1 - e^{\nu^{-} \cdot P_{max}}} \cdot \left(1 - e^{\nu^{-} \cdot (P - P_{max})}\right) + \sigma \tag{12}$$

where $G^{+}$and G^{-} are the normalized conductances of LTP and LTD, respectively; ν^{+} and ν^{-} are the nonlinearity coefficients of LTP and LTD, respectively; P_{max} is the maximum pulse number; and σ is the noise of each conductance value sampled from a normal distribution to approximate the cycle-to-cycle and device-to-device variations.[42] To handle the negative weight values, a differential method with two devices was adopted. The ANN weight (w) was defined as $w = G^{+} + G^{-} - 0.1$. When updating the weights with the LTP or LTD conductance, only a single pulse was applied to the device for power efficiency, and the conductance changes of LTP and LTD were unidirectional. Furthermore, a reset mechanism was applied to stabilize the training process when the conductance reached the last stage of LTP or LTD. Figure 6c shows the fitted LTP and LTD curves; the nonlinearity coefficients for LTP (ν^{+}) and LTD (ν^{-}) were 0.0005 and − 0.002, respectively. The coefficient of the ideal case was zero, which represents perfectly linear LTP and LTD curves. Figure 6d illustrates the accuracy curves of the proposed device and the ideal case using digit MNIST; the accuracy for the digits MNIST was 96.55% which is close to the ideal value of 97.15% Figure 6e presents the accuracy performance on the Fashion MNIST dataset, where the proposed device was also evaluated. Despite using a non-linear curve, we were able to optimize effectively and achieve higher accuracy than the ideal in Fashion MNSIT. Figure S16 (Supporting Information) reveals the recognition accuracy for different classes, indicating high accuracy for digits 0 and 1 in digit MNIST and trousers, sneakers, and bags in Fashion MNIST, highlighting the model's effective class distinction. The simulation results of

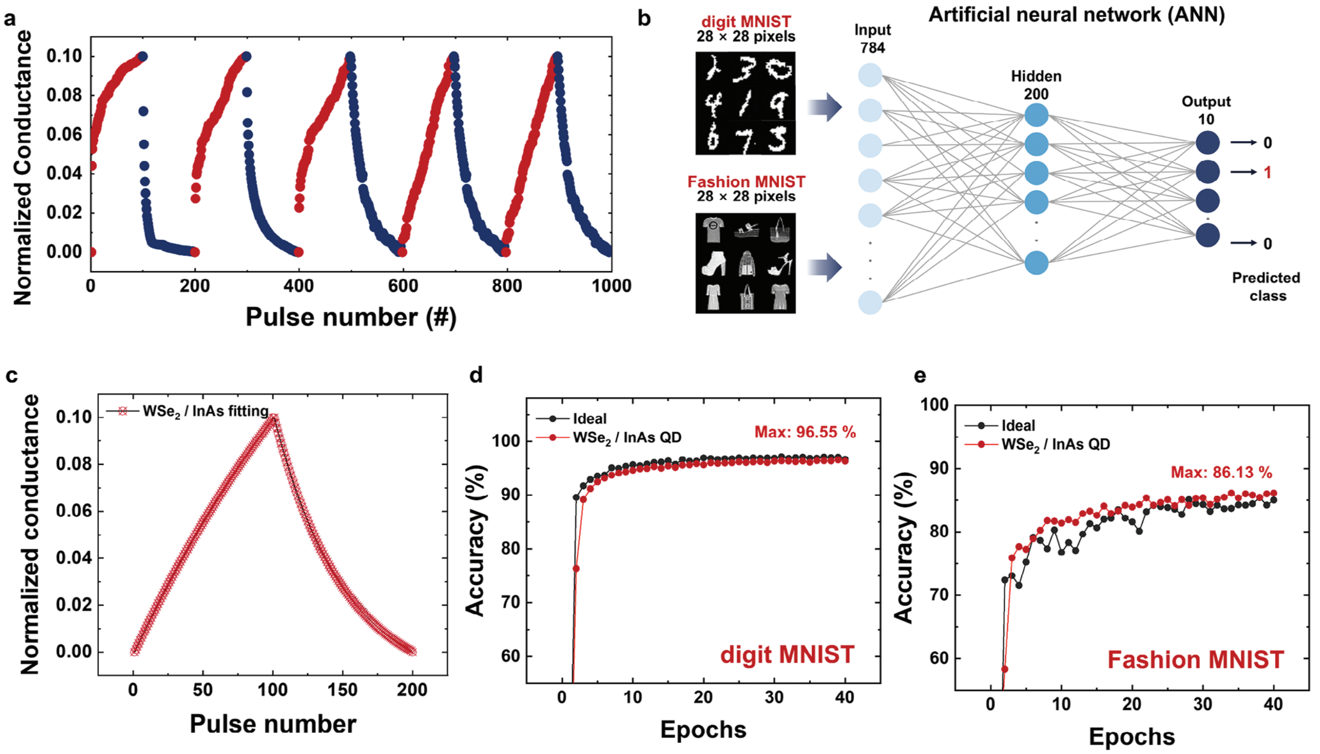

Figure 6. Short-wavelength infrared-triggered neuromorphic behavior and image recognition. a) Potentiation and depression properties of WSe_2/InAs with gate voltages of −20 V and +20 V under 5 mW laser illumination. b) Schematic of ANN training for classification of the digit MNIST and the Fashion MNIST dataset. c) Fitting of WSe_2/InAs LTP and LTD curves for simulations. d) The recognition rate of the simulated digit MNIST using experimental data. e) The recognition rate of the simulated Fashion MNIST using experimental data.

our device demonstrate above-average image recognition accuracy on the MNIST and Fashion MNIST datasets, as shown in Table S3. The present approach achieves state-of-the-art results with a more compact architecture among differential methods using backpropagation (BP). We performed ablation studies to enhance our model's performance by varying the number of neurons in the hidden layer. This optimization resulted in an accuracy of 86.13% on Fashion MNIST, setting a new state-of-the-art benchmark among differential methods using BP, as detailed in Table S4, Supporting Information. Figure 6e shows the confusion matrix of the pre-trained ANN model, visualizing the network's correct and incorrect predictions on each class. Specifically, the pre-trained ANN model classified the "Trouser" and "Ankle Boot" classes but was less effective at detecting the "Shirt" and "Pullover" classes. This simulation verified the effectiveness of our device in artificial intelligence applications.

To assess the potential of the device developed in this study as a practical machine vision device, we measured the power consumption at a minimum pulse width of 100 ms, which exhibits synaptic behavior, by extracting values from Figure S17 (Supporting Information) and using the following equation.[32a]

$$E = V_{AM} \cdot EPSC \cdot t_{pw} \tag{13}$$

The device demonstrated a low power consumption of 33.5 pJ. Despite having a channel width of only 10 μm, the device can still exhibit a current increase upon optical stimulation, making it suitable for miniaturization and a promising candidate for the development of machine vision technology.

3. Conclusion

Our WSe_2/InAs QD heterostructure exhibited an enhanced photoresponse in the SWIR region compared with that of the pristine WSe_2 device. The integration of InAs QDs into the WSe_2 synapse device enhanced IR responsivity and synaptic behavior, consistent with retinomorphic transistors based on multi-dimensional heterojunctions. The WSe_2 channel structure facilitated efficient charge transport, whereas the InAs QDs provided quantum confinement effects that enhanced IR photon absorption, thereby improving the detection capabilities. The engineered WSe_2/InAs vdW heterojunction device exhibited sensitivity across a wide range of IR wavelengths over 1000 nm, making it suitable for sensing applications associated with both longer IR and shorter visible and near-IR wavelengths. The integration of QDs with 2D materials enhanced their local photon capture capabilities and overall photodetector efficiency, thus overcoming the limitations of the 2D materials. The heterojunction facilitated effective separation of photoexcited electron-hole pairs, further enhancing the photodetector performance. Our WSe_2/InAs retinomorphic device adapted to the SWIR signal intensity variations, similar to the human eye's adaptation to changes in ambient light intensity in the visible-light range. Moreover, the trained ANN achieved a >86% inference accuracy in the Fashion MNIST dataset, which was encoded into spikes by the device. The WSe_2/InAs vdW heterojunction device extends sensitivity to the SWIR region, surpassing the visible spectrum range of conventional retina-inspired systems. It combines neuromorphic functionality with high responsivity (1.134 A/W) and tunable synaptic plasticity (LTP/LTD, STDP), accurately mimicking retina adaptation under visible and IR light intensities. Additionally, the device offers enhanced stability, lower power consumption, and improved scalability, addressing the limitations of state-of-the-art systems technologies. These advancements mark significant progress in retina-inspired optoelectronics for machine vision and in-sensor computing applications.

4. Experimental Section

Materials: Indium (III) chloride (anhydrous, 99.999%) was purchased from Strem Chemicals. Arsenic (III) chloride (99.99%, trace metals basis), oleylamine (OLAM, 70%, technical grade), lithium triethylborohydride ($LiEt_3BH$, superhydride, 1.0 M solution in THF), dioctyl ether (DOE, 99%), tetrachloroethylene (TCE, anhydrous, ≥99%), EDT (technical grade, ≥90%), acetonitrile (anhydrous, 99.8%), toluene (anhydrous, 99.8%), and octane (anhydrous, ≥ 99%) were purchased from Sigma-Aldrich.

Synthesis of InAs QDs: The InAs QDs were synthesized by a modified co-reduction method using an As precursor and OLAM.[19] In a glovebox, $InCl_3$ (1 mmol) and $AsCl_3$ (5 mmol) were dissolved in 20 mL of pre-degassed OLAM by stirring overnight at 60 °C. In a three-necked flask under an inert atmosphere, 0.5 and 0.25 mmol of the $InCl_3$ and $AsCl_3$ were mixed. To this mixture, 2.5 mmol of superhydride in pre-degassed DOE was injected. Then, the reaction flask was heated gradually to the reaction temperature at a heating rate of 3 °C min^{-1} and maintained at that temperature for 15 min. After the completion of the growth process, the reaction was quickly stopped, and the product was transferred to a glovebox to avoid exposure to air. For purification, 30 mL of toluene was added to the reaction mixture, which was then divided into two centrifuge tubes. The dispersions were centrifuged at 5000 rpm for 5 min. Acetonitrile was added to each supernatant until it became turbid, and the dispersions were centrifuged again in the same manner. The resulting aggregates were dissolved in toluene, and ethanol was added to the dispersions. The dispersions were centrifuged for the last time, and the resultant aggregates were re-dispersed in octane.

Fabrication of Synaptic Devices: For the p-type channel, a WSe_2 film was transferred onto the SiO_2/heavily p-doped Si substrate without thermal fatigue. UV lithography and an electron-beam evaporator were used to fabricate Ni electrodes on top of the WSe_2 film for the postsynaptic terminal. Finally, the InAs QDs were spin-coated on the Ni/WSe_2/SiO_2 substrate using the EDT method at 2000 rpm for 30 s. The resultant hybrid WSe_2/InAs photodetector was baked for 30 min at 150 °C. For the ligand exchange of QDs with EDT, the EDT solution was applied to the InAs QD film for 30 s and then spin-coated at 2000 rpm for 30 s. Then, acetonitrile solution was spin-coated on the EDT-treated InAs QD film at 2000 rpm for 5 s two times and 30 s one time, and the resultant film was baked for 30 min at 150 °C.

Device Characterization: For the UV-vis-SWIR absorption measurements, the synthesized InAs QDs were dispersed in octane and spin-coated onto a glass substrate. WSe_2 was deposited on a glass substrate. The absorption spectra were obtained using a SHIMADZU UV-2600 instrument in the range of 200–1400 nm. XRD measurements were conducted using a miniFlex 600 diffractometer (RIGAKU) with a Cu Kα source at 40 kV and 15 mA. TEM was performed using a JEOL JEM-2010 system at 200 kV. Raman spectra were acquired using a DXR2xi instrument (Thermo Fisher Scientific) with a 532 nm laser at 6.1 mW power. UPS measurements were conducted using an XPS-Theta Probe (Thermo Fisher Scientific).

The electrical and photoresponse properties of the photodetector were analyzed using a semiconductor parameter analyzer connected to a probe station. The transfer characteristics were measured by applying a drain bias of 1 V with a back-gate bias sweep from −50 to 50 V. To measure the photocurrent of the pristine WSe_2 and WSe_2/InAs vdW heterojunction device, a laser of 1060 nm was used as the SWIR light source. To measure the output characteristics of the WSe_2/InAs vdW heterojunction device, the drain and gate biases were swept from −10 to 10 V and −40 to 40 V, respectively, in steps of 10 V. To analyze the responsivity of the devices, they were irradiated with a SWIR laser at a distance of 0.5 cm, which led to the formation of a circular pattern of 0.7 cm diameter.

Supporting Information

Supporting Information is available from the Wiley Online Library or from the author.

Acknowledgements

This study was supported by National Research Foundation of Korea (NRF) grants funded by the Government of the Republic of Korea (2021R1C1C1012209, RS-2023-00275300). N.O. acknowledges the financial support from an NRF grant funded by the Government of the Republic of Korea (RS-2024-00358337), the US Army Combat Capabilities Development Command Soldier Center (DEVCOM SC), and the International Technology Center Pacific (ITC PAC) Global Research Project. This work was supported by the Glocal University 30 Project Fund of Gyeongsang National University in 2024. It also noted that atomic layer deposition (ISAC iOV dX1) was used for device fabrication, at Gyeongsang National University.

Conflict of Interest

The authors declare no conflict of interest.

Author Contributions

S.S., S.K., and D.L. contributed equally to this work. S.S. and S.K. prepared the materials for most of the experimental measurements and analyzed the results. S.S., S.K., N.O., and J.H.P. conceived and designed the study. H.K., M.J.K., S.C., W.A.L., J.S., and S.S.K. assisted with the physicochemical characterization and optical instrumentation. D.L. performed the CNN simulation, and S.S., S.K., N.O., and J.H.P. prepared the manuscript. All authors discussed the results and commented on the manuscript. All authors revised and commented on the manuscript. N.O. and J.H.P. supervised this study.

Data Availability Statement

The data that support the findings of this study are available from the corresponding author upon reasonable request.

Keywords

2D materials, artificial visual system, retinomorphic synapse device, short-wavelength infrared, van der Waals heterojunction

Received: November 15, 2024
Revised: January 26, 2025
Published online: March 3, 2025

[1] E. Zrenner, *Science* **2002**, *295*, 1022.
[2] C. Li, W. Du, Y. Huang, J. Zou, L. Luo, S. Sun, A. O. Govorov, J. Wu, H. Xu, Z. Wang, *Opto-Electron. Adv.* **2022**, *5*, 210069.

[3] J. Zhang, P. Guo, Z. Guo, L. Li, T. Sun, D. Liu, L. Tian, G. Zu, L. Xiong, J. Zhang, J. Huang, *Adv. Funct. Mater.* **2023**, *33*, 2302885.
[4] M. M. Islam, A. Krishnaprasad, D. Dev, R. Martinez-Martinez, V. Okonkwo, B. Wu, S. S. Han, T. S. Bae, H. S. Chung, J. Touma, Y. Jung, T. Roy, *ACS Nano* **2022**, *16*, 10188.
[5] Z. Zhang, X. Liu, H. Zhou, S. Xu, C. Lee, *Small Struct.* **2023**, *5*, 2300325.
[6] D. J. Blumenthal, *APL Photonics* **2020**, *5*, 020903.
[7] Y. Zhao, L. Cheng, R. Xu, Z. Yu, J. Zhang, *Brain-X* **2024**, *2*, e70004.
[8] a) T. Chu, H. Ilatikhameneh, G. Klimeck, R. Rahman, Z. Chen, *Nano Lett.* **2015**, *15*, 8000; b) X. Duan, C. Wang, A. Pan, R. Yu, X. Duan, *Chem. Soc. Rev.* **2015**, *44*, 8859; c) Y. Zhao, K. Xu, F. Pan, C. Zhou, F. Zhou, Y. Chai, *Adv. Funct. Mater.* **2016**, *27*, 1603484.
[9] J. Gusakova, X. Wang, L. L. Shiau, A. Krivosheeva, V. Shaposhnikov, V. Borisenko, V. Gusakov, B. K. Tay, *Phys. Status Solidi* **2017**, *214*, 1700218.
[10] D. V. Talapin, J.-S. Lee, M. V. Kovalenko, E. V. Shevchenko, *Chem. Rev.* **2010**, *110*, 389.
[11] a) C. R. Kagan, E. Lifshitz, E. H. Sargent, D. V. Talapin, *Science* **2016**, *353*, 5523; b) B. Sun, A. M. Najarian, L. K. Sagar, M. Biondi, M. J. Choi, X. Li, L. Levina, S. W. Baek, C. Zheng, S. Lee, A. R. Kirmani, R. Sabatini, J. Abed, M. Liu, M. Vafaie, P. Li, L. J. Richter, O. Voznyy, M. Chekini, Z. H. Lu, F. P. Garcia de Arquer, E. H. Sargent, *Adv. Mater.* **2022**, *34*, 2203039.
[12] a) B. K. Jung, H. Yoo, B. Seo, H. J. Choi, Y. K. Choi, T. H. Kim, N. Oh, S. Y. Kim, S. Kim, Y. Lee, J. W. Shim, H. Y. Park, G. W. Hwang, T. N. Ng, S. J. Oh, *ACS Energy Lett.* **2024**, *9*, 504; b) Y. Kim, J. H. Chang, H. Choi, Y. H. Kim, W. K. Bae, S. Jeong, *Chem. Sci.* **2019**, *11*, 913; c) P. Reiss, M. Carriere, C. Lincheneau, L. Vaure, S. Tamang, *Chem. Rev.* **2016**, *116*, 10731.
[13] a) J. Zha, M. Luo, M. Ye, T. Ahmed, X. Yu, D. H. Lien, Q. He, D. Lei, J. C. Ho, J. Bullock, K. B. Crozier, C. Tan, *Adv. Funct. Mater.* **2021**, *32*, 2111970; b) Y. Cheng, H. Li, B. Liu, L. Jiang, M. Liu, H. J. Yang, J. He, J. Jiang, *Small* **2020**, *16*, 2005217; c) H. Yang, W. Fan, A. Vaneski, A. S. Susha, W. Y. Teoh, A. L. Gogach, *Adv. Funct. Mater.* **2012**, *22*, 2821.
[14] a) J. Huang, J. Ding, F. Tan, Y. Gao, X. Lu, C. Dong, G. Yue, X. Xu, L. Ding, *J. Mater. Chem. C* **2023**, *11*, 17106; b) G. Konstantatos, M. Badioli, L. Gaudreau, J. Osmond, M. Bernechea, F. P. Garcia de Arquer, F. Gatti, F. H. Koppens, *Nat. Nanotechnol.* **2012**, *7*, 363; c) X. Tang, M. Chen, A. Kamath, M. M. Ackerman, P. Guyot-Sionnest, *ACS Photonics* **2020**, *7*, 1117; d) Q. Zhang, F. Yang, S. Zhou, N. Bao, Z. Xu, M. Chaker, D. Ma, *Appl. Catal., B* **2020**, *270*, 118879.
[15] M. Yang, Z. Luo, W. Gao, M. Zhang, L. Huang, Y. Zhao, J. Yao, F. Wu, J. Li, Z. Zheng, *Adv. Opt. Mater.* **2022**, *10*, 2200717.
[16] Z. Zheng, J. Yao, G. Yang, *ACS Appl. Mater. Interfaces* **2017**, *9*, 7288.
[17] a) C. Choi, J. Leem, M. Kim, A. Taqieddin, C. Cho, K. W. Cho, G. J. Lee, H. Seung, H. J. Bae, Y. M. Song, T. Hyeon, N. R. Aluru, S. Nam, D. H. Kim, *Nat. Commun.* **2020**, *11*, 5934; b) Y. Fan, Y. Wang, X. Hao, W. Deng, Z. Jin, *J. Colloid Interface Sci.* **2024**, *672*, 700; c) B. Sun, T. Guo, G. Zhou, S. Ranjan, Y. Jiao, L. Wei, Y. N. Zhou, Y. A. Wu, *Mater. Today Phys.* **2021**, *18*, 100393; d) S. Yadav, S. R. Jena, B. M. B., A. Altaee, M. Saxena, A. K. Samal, *Emergent Mater.* **2021**, *4*, 901.
[18] B. Bae, M. Park, D. Lee, I. Sim, K. Lee, *Adv. Opt. Mater.* **2022**, *11*, 2201905.
[19] a) S. Kim, S. Yeon, M. Lee, J. Jin, S. Shin, N. Gwak, I. Jeong, H. Jang, G. W. Hwang, N. Oh, *NPG Asia Mater* **2023**, *30*, 2310671; b) T. Zhao, N. Oh, D. Jishkariani, M. Zhang, H. Wang, N. Li, J. D. Lee, C. Zeng, M. Muduli, H. J. Choi, D. Su, C. B. Murray, C. R. Kagan, *J. Am. Chem. Soc.* **2019**, *141*, 15145.
[20] a) E.d. Corro, H. Terrones, C. F. Ana Elias, S. Feng, M. A. Nguyen, T. E. Mallouk, M. Terrones, M. A. Pimenta, *ACS Nano* **2014**, *8*, 9629; b) H. Terrones, E. Del Corro, S. Feng, J. M. Poumirol, D. Rhodes, D. Smirnov, N. R. Pradhan, Z. Lin, M. A. Nguyen, A. L. Elias, T. E. Mallouk, L. Balicas, M. A. Pimenta, M. Terrones, *Sci. Rep.* **2014**, *4*, 4215; c) M. Yamamoto, S. T. Wang, M. Ni, Y.-F. Lin, S.-L. Li, S. Aikawa, W.-B. Jian, K. Ueno, K. Wakabayashi, K. Tsukagoshi, *ACS Nano* **2014**, *8*, 3895; d) W. Zhao, Z. Ghorannevis, K. K. Amara, J. R. Pang, M. Toh, X. Zhang, C. Kloc, P. H. Tan, G. Eda, *Nanoscale* **2013**, *5*, 9677.
[21] Y. Zhao, K. Lu, J. Yao, J. Ning, B. Chen, H. Lu, C. Zheng, *Sci. Rep.* **2023**, *13*, 123.
[22] N. Dong, Y. Li, Y. Feng, S. Zhang, X. Zhang, C. Chang, J. Fan, L. Zhang, J. Wang, *Sci. Rep.* **2015**, *5*, 14646.
[23] Y. Hu, H. Yang, J. Huang, X. Zhang, B. Tan, H. Shang, S. Zhang, W. Feng, J. Zhu, J. Zhang, Y. Shuai, D. Jia, Y. Zhou, P. Hu, *ACS Appl. Mater. Interfaces* **2022**, *14*, 55839.
[24] S. S. Kundale, H. Kim, D. D. Kumbhar, C.-H. Oh, S.-Y. Cho, M. J. Kwon, S. Shim, W. Kim, S. Mukherjee, S. W. Kim, J. H. Park, *ACS Mater. Lett.* **2024**, *6*, 3384.
[25] Q. Wang, R. Jiang, Z. Gao, M. Deng, J. Chen, L. Zhu, L. Shang, Y. Li, D. Fuchs, J. Zhang, Z. Hu, *Appl. Surf. Sci.* **2023**, *613*, 156148.
[26] a) S. Chuang, R. Kapadia, H. Fang, T. C. Chang, W.-C. Yen, Y.-L. Chueh, A. Javey, *Appl. Phys. Lett.* **2013**, *102*, 242101; b) Y. X. Hou, Y. Li, Z. C. Zhang, J. Q. Li, D. H. Qi, X. D. Chen, J. J. Wang, B. W. Yao, M. X. Yu, T. B. Lu, J. Zhang, *ACS Nano* **2021**, *15*, 1497.
[27] H. J. Yun, J. Lim, J. Roh, D. C. J. Neo, M. Law, V. I. Klimov, *Nat. Commun.* **2020**, *11*, 5280.
[28] J. Zou, Y. Ke, X. Zhou, Y. Huang, W. Du, L. Lin, S. Wei, L. Luo, H. Liu, C. Li, K. Shen, A. Ren, J. Wu, *Adv. Opt. Mater.* **2022**, *10*, 2200143.
[29] S. H. Kim, D. Lee, S. Moon, J. H. Choi, D. Kim, J. Kim, S. W. Baek, *Adv. Funct. Mater.* **2023**, *33*, 2303778.
[30] a) K. K. Manga, J. Wang, M. Lin, J. Zhang, M. Nesladek, V. Nalla, W. Ji, K. P. Loh, *Adv. Mater.* **2012**, *24*, 1697; b) W. Deng, Z. Zheng, J. Li, R. Zhou, X. Chen, D. Zhang, Y. Lu, C. Wang, C. You, S. Li, L. Sun, Y. Wu, X. Li, B. An, Z. Liu, Q. J. Wang, X. Duan, Y. Zhang, *Nat. Commun.* **2022**, *13*, 4627; c) K. Zhang, X. Fang, Y. Wang, Y. Wan, Q. Song, W. Zhai, Y. Li, G. Ran, Y. Ye, L. Dai, *ACS Appl. Mater. Interfaces* **2017**, *9*, 5392; d) Y. Xin, X. Wang, Z. Chen, D. Weller, Y. Wang, L. Shi, X. Ma, C. Ding, W. Li, S. Guo, R. Liu, *ACS Appl. Mater. Interfaces* **2020**, *12*, 15406; e) J. Schornbaum, B. Winter, S. P. Schießl, F. Gannott, G. Katsukis, D. M. Guldi, E. Spiecker, J. Zaumseil, *Adv. Funct. Mater.* **2014**, *24*, 5798; f) B. C. Hsu, S. T. Chang, T. C. Chen, P. S. Kuo, P. S. Chen, Z. Pei, C. W. Liu, *IEEE Electron Device Lett.* **2003**, *24*, 318; g) L. Ye, H. Li, Z. Chen, J. Xu, *ACS Photonics* **2016**, *3*, 692.
[31] K. Liang, R. Wang, B. Huo, H. Ren, D. Li, Y. Wang, Y. Tang, Y. Chen, C. Song, F. Li, B. Ji, H. Wang, B. Zhu, *ACS Nano* **2022**, *16*, 8651.
[32] a) T. Kim, K. S. Yun, *Sci. Rep.* **2023**, *13*, 12583; b) Y. Wang, K. Wang, X. Hu, Y. Wang, W. Gao, Y. Zhang, Z. Liu, Y. Zheng, K. Xu, D. Yang, X. Pi, *ACS Nano* **2023**, *17*, 3696; c) P. Zhao, X. Peng, M. Cui, Y. Li, C. Jiang, C. Luo, B. Tian, H. Lin, H. Peng, C.-G. Duan, *ACS Appl. Polym. Mater* **2023**, *5*, 8764.
[33] C. Blauth, P. Mulvaney, T. Hirai, *Appl. Phys. Lett.* **2019**, 115.
[34] Y. Xi, B. Gao, J. Tang, A. Chen, M.-F. Chang, X. S. Hu, J. V. D. Spiegel, H. Qian, H. Wu, *Proc. IEEE* **2021**, *109*, 14.
[35] Y. Zhang, L. Liu, B. Tu, B. Cui, J. Guo, X. Zhao, J. Wang, Y. Yan, *Nat. Commun.* **2023**, *14*, 247.
[36] a) C. Jo, J. Kim, J. Y. Kwak, S. M. Kwon, J. B. Park, J. Kim, G. S. Park, M. G. Kim, Y. H. Kim, S. K. Park, *Adv. Mater.* **2022**, *34*, 2108979; b) A. Thomas, A. N. Resmi, A. Ganguly, K. B. Jinesh, *Sci. Rep.* **2020**, *10*, 12450.
[37] a) G. Billings, M. C. van Rossum, *J. Neurophysiol.* **2009**, *101*, 2775; b) S. Subramanian Periyal, M. Jagadeeswararao, S. E. Ng, R. A. John, N. Mathews, *Adv. Mater. Technol.* **2020**, *5*, 2000514.

[38] S. S. Kundale, P. S. Pawar, D. D. Kumbhar, I. K. G. Devara, I. Sharma, P. R. Patil, W. A. Lestari, S. Shim, J. Park, T. D. Dongale, S. Y. Nam, J. Heo, J. H. Park, *Adv. Sci.* **2024**, *11*, 2405251.
[39] R. C. Curby, D. K. Ferry, *Phys. Rev. B* **1971**, *3*, 3379.
[40] K. J. Burke Jr., K. J. Bender, *Front. Cell Neurosci.* **2019**, *13*, 221
[41] H. Xiao, K. Rasul, R. Vollgraf, arXiv preprint arXiv:1708.07747.
[42] a) T. Jin, Y. Zheng, J. Gao, Y. Wang, E. Li, H. Chen, X. Pan, M. Lin, W. Chen, *ACS Appl. Mater. Interfaces* **2021**, *13*, 10639; b) J. Tang, C. He, J. Tang, K. Yue, Q. Zhang, Y. Liu, Q. Wang, S. Wang, N. Li, C. Shen, Y. Zhao, J. Liu, J. Yuan, Z. Wei, J. Li, K. Watanabe, T. Taniguchi, D. Shang, S. Wang, W. Yang, R. Yang, D. Shi, G. Zhang, *Adv. Funct. Mater.* **2021**, *31*, 2011083; c) M. Kim, M. A. Rehman, D. Lee, Y. Wang, D. H. Lim, M. F. Khan, H. Choi, Q. Y. Shao, J. Suh, H. S. Lee, H. H. Park, *ACS Appl. Mater. Interfaces* **2022**, *14*, 44561; d) D. D. Kumbhar, Y. Je, S. Hong, D. Lee, H. Kim, M. J. Kwon, S. Y. Cho, D. H. Lee, D. H. Lim, S. Kim, J. H. Park, *Adv. Funct. Mater.* **2024**, *34*, 2311994; e) H. Cho, D. Lee, K. Ko, D. Y. Lin, H. Lee, S. Park, B. Park, B. C. Jang, D. H. Lim, J. Suh, *ACS Nano* **2023**, *17*, 7384.

